Asian Journal of Pharmaceutical Sciences 17 (2022) 557–570

Available online at www.sciencedirect.com

ScienceDirect

journal homepage: www.elsevier.com/locate/AJPS

Original Research Paper

Non-cytotoxic nanoparticles re-educating macrophages achieving both innate and adaptive immune responses for tumor therapy

Shengmei Wang[a,d,1], *Xuanjun Liu*[a,b,1], *Minghua Yang*[c], *Linqi Ouyang*[d], *Jinsong Ding*[b], *Shengfeng Wang*[a,b,c,*], *Wenhu Zhou*[a,b,*]

[a] *Department of Pharmacy, The Third Xiangya Hospital, Central South University, Changsha, Hunan, 410013, China*
[b] *Xiangya School of Pharmaceutical Sciences, Central South University, Changsha, Hunan, 410013, China*
[c] *Postdoctoral Research Station of Clinical Medicine and Department of Pediatrics, The Third Xiangya Hospital, Central South University, Changsha, Hunan, 410013, China*
[d] *The First Hospital of Hunan University of Chinese Medicine, Changsha, Hunan, 410007, China*

ARTICLE INFO

Article history:
Received 14 January 2022
Revised 3 June 2022
Accepted 5 June 2022
Available online 10 June 2022

Keywords:
Core-shell nanoparticles
Metal-organic-framework
CpG
IPI549
Tumor immunotherapy

ABSTRACT

Macrophages are important antigen-presenting cells to combat tumor via both innate and adaptive immunity, while they are programmed to M2 phenotype in established tumors and instead promote cancer development and metastasis. Here, we develop a nanomedicine that can re-educate M2 polarized macrophages to restore their anti-tumor activities. The nanomedicine has a core-shell structure to co-load IPI549, a PI3Kγ inhibitor, and CpG, a Toll-like receptor 9 agonist. Specifically, the hydrophobic IPI549 is self-assembled into a pure drug nano-core, while MOF shell layer is coated for CpG encapsulation, achieving extra-high total drugs loading of 44%. Such nanosystem could facilitate intracellular delivery of the payloads but without any cytotoxicity, displaying excellent biocompatibility. After entering macrophages, the released IPI549 and CpG exert a synergistic effect to switch macrophages from M2 to M1 phenotype, which enables anti-tumor activities via directly engulfing tumor cells or excreting tumor killing cytokines. Moreover, tumor antigens released from the dying tumor cells could be effectively presented by the re-educated macrophages owing to the up-regulation of various antigen presenting mediators, resulting in infiltration and activation of cytotoxic T lymphocytes. As a result, the nanosystem triggers a robust anti-tumor immune response in combination with PD-L1 antibody to inhibit tumor growth and metastasis. This work provides a non-cytotoxic nanomedicine to modulate tumor immune microenvironment by reprograming macrophages.

* Corresponding authors.
E-mail address: zhouwenhuyaoji@163.com (W.H. Zhou).
[1] These authors contributed equally to this work.
Peer review under responsibility of Shenyang Pharmaceutical University.

https://doi.org/10.1016/j.ajps.2022.06.001

1. Introduction

Immunotherapy has emerged as the most promising method to treat malignant tumors, which functions by activating the body's immune system to attack tumor cells [1,2]. This is an unprecedentedly rapid developing field, and a number of pharmacological treatments have been available in clinic, such as immune checkpoint blockade (ICB) therapy and chimeric antigen receptor (CAR) T cell therapy. However, while the development of ICB therapies (e.g., CTLA-4 and PD-1/PD-L1 antibodies) has revolutionized cancer treatment, the overall response rate in clinic is still rather limited, benefiting for less than 30% of patients [3,4]. Because of the complexity of the tumor microenvironment, the efficacy of ICB can be affected by various factors, such as inadequate tumor immunogenicity, insufficient infiltration of immune cells, and immunosuppressive tumor microenvironment (ITM) [5–7]. The anti-tumor immune response contains a continuous multiple steps including antigen presentation (Phase I), lymphocyte activation, proliferation and differentiation (Phase II), and tumor elimination (Phase III) [8]. This is a cascade process, in which the restriction of any step would compromise the overall efficacy. The current ICB therapies mainly focus on the final step to promote the elimination of tumor cells by effector T cells, while the limitations of Phase I/II are usually ignored. Actually, the efficiency of Phase I/II is closely related to the activity of antigen-presenting cells (APCs), a type of immune cells that bridges innate and adaptive immunity [9]. The APCs could exert their innate immunity via directly engulfing tumor cells or excreting anti-tumor cytokines, and the dying cancer cells' antigens can be captured and presented by APCs for the activation of adaptive immunity [10]. Therefore, in addition to effector T cells, the APCs are another important target that should be taken into consideration for anti-tumor immunotherapy.

Macrophages are the most abundant APCs that account for ~50% of the tumor mass in solid tumors [11]. Macrophages are mainly differentiated from monocytes, and the infiltration of macrophages plays critical roles in tumor development, progress, and development [12]. Dependent on the stimulations they receive, macrophages can differentiate into various phenotypes with extremely different functions, with two major subtypes of the classical activated M1 macrophages and alternative activated M2 macrophages [13]. In early stage of tumor formation, macrophages tend to polarize into M1, which secretes pro-inflammatory cytokines to aid the tumor cell clearance [14]. However, with the tumor progress, the ITM polarizes macrophages into M2 type tumor associated macrophages (TAM) to promote tumor growth [15]. The level of M2 type macrophages infiltration into tumor is highly correlated with poor outcomes of immunotherapy [16]. Fortunately, the polarized macrophages are plastic, which can undergo phenotype switch upon different treatments. For example, the M2-type macrophages can be reversed into M1 macrophages by certain stimuli to recover their anti-tumor activities [17]. Given critical roles of macrophages in cancer immunity and their plasticity, various macrophages-targeting strategies have been developed to modulate macrophages against cancer, such as macrophage depletion and inhibition, macrophage repolarization, as well as the enhancement of its immune function (e.g., phagocytosis) [18]. While strategies to inhibit/deplete TAMs have made real clinic impact [19], macrophages reprogramming is more attractive in fundamental studies since it can regulate ITM with minimal side-effects to synergize ICB for enhanced immunotherapy [11].

Recent years have witnessed a surge in development of nanomedicines to educate macrophages [20,21]. A notable advantage of nano-drug delivery systems is their capability to allow tumor accumulation, cell-targeting delivery, and sustained drug release via appropriate structure and surface modifications. Various small molecular drugs [22, 23], cytokines [24], and nucleic acids [25] have been delivered by nanoparticles to reprogram TAM into M1 phenotypes, which restores their tumor killing and antigen presenting activities. However, the current efficacy of macrophage-regulating systems is not satisfactory in several animal models, likely due to the cunning tumor cells that can protect them from immune attack through various immune escape mechanisms. For example, cancer cells can express a "don't eat me" signal called CD47 on the cellular surface, which binds signal regulatory protein alpha (SIRPα) receptor on macrophages to avoid phagocytosis [26]. To overcome this, extra CD47 antagonists are required to promote macrophages swallowing the cancer cells [27]. Moreover, many tumors have "cold" immune microenvironment with poor exposure of tumor-associated antigens [28]. To this end, extensive efforts have been made to increase antigen exposure in tumor, and it is found that several chemotherapeutics (such as doxorubicin, paclitaxel and oxaliplatin) [29,30], phototherapies [31,32], and radiotherapy [33,34] could induce immunogenic cell death (ICD) to release tumor antigens. Upon ICD stimulation, tumor cells can release tumor-associated antigens (TAA) to allow the antigen presentation of macrophages, which subsequently activates cytotoxic T lymphocytes to suppress tumor [35]. However, while these combinations are effective to enhance anti-tumor immune response, complicated nanosystems are required to deliver and release multiple cargoes in tumor, which enter different cells to exert their respective functions. Moreover, the ICD-triggering agents may cause undesirable side-effects [36]. Besides systematic toxicity, the ICD-induced over-generation of immunogenicity could cause inflammatory response and even cytokine storm with multiple organ failures [37]. Despite significant advances in the field, there still lacks of simple yet robust macrophage regulating method to simultaneously damage tumor cells, capture and present tumor antigens, and activate effector T cells for enhanced immunotherapy.

Herein, we report a nanomedicine to activate both innate and adaptive immune responses of macrophages for tumor therapy. The nanoparticles have a pure drug core of IPI549, and a metal-organic-framework (MOF) shell layer to co-load CpG oligodeoxynucleotide (Scheme 1). IPI549 is a highly selective phosphoinositide-3-kinase-gamma (PI3Kγ) inhibitor, which has entered clinical trials to treat various types of solid tumor (NCT02637531, NCT03795610) [38]. IPI549 could regulate ITM by reprograming macrophages from M2 to M1 phenotype, and showed synergistic anti-tumor effect in animal model in combination with ICB [39,40]. CpG is

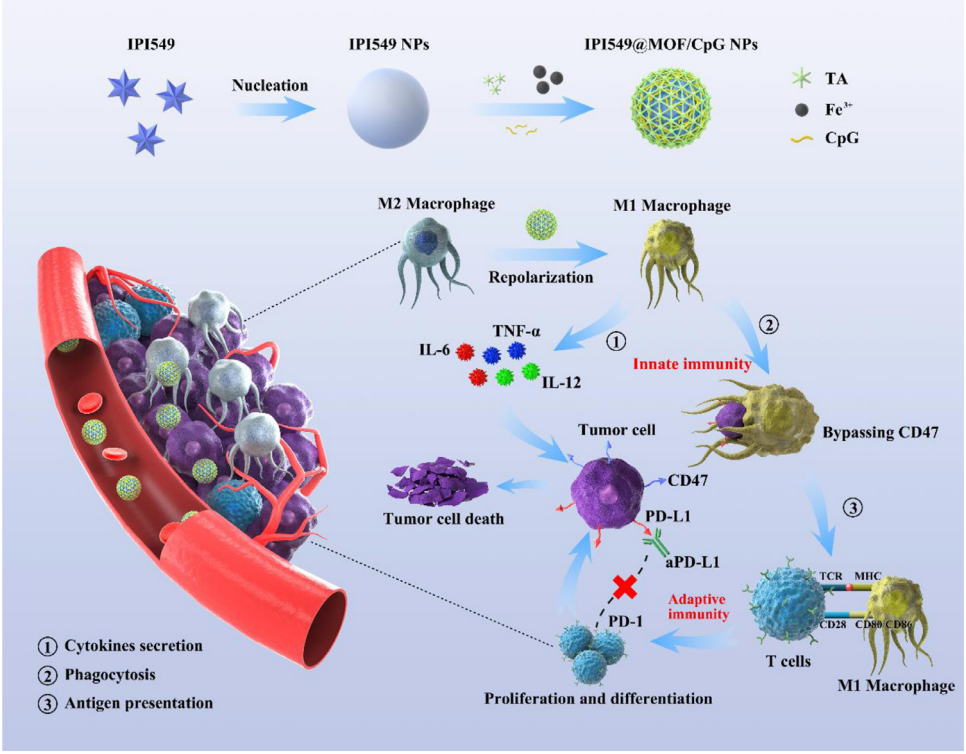

Scheme 1 – Schematic showing the preparation of nanomedicine to co-load IPI549 and CpG, and its mechanism to re-educate macrophages for anti-tumor therapy.

a short, synthetic single-stranded DNA molecule, which also displays a strong immunostimulatory effect via its binding to pattern-recognition receptor Toll-like receptor 9 (TLR9) in macrophages [41]. Through a simple self-assembly process, IPI549 and CpG could be co-loaded into the nanoparticles with total drug loading capacity over 40%. Such nanosystem is highly biocompatible with non-cytotoxicity towards both tumor cells and macrophages. After delivering into macrophages, IPI549 and CpG work synergistically to switch the cells from M2 type to M1. The re-educated M1 macrophages excrete pro-inflammatory cytokines to modulate the ITM and inhibit tumor cells, and notably, bypass the CD47-SIRPα blockage pathway to engulf tumor cells owing to the capability of CpG to evoke changes in the central carbon metabolism of macrophages [42]. Meanwhile, CD80/CD86 and major histocompatibility complex class II (MHC II) molecules are up-regulated in macrophages surface, which facilitate the presentation of tumor antigen released from the dying tumor cells. Collectively, such nanoparticles could effectively activate the Phase I/II steps of anti-tumor immune response, which combines ICB to inhibit tumor growth and metastasis via cancer immunotherapy.

2. Materials and methods

2.1. *Materials*

IPI549 was purchased from MedChemExpress LLC (New Jersey, USA). Ferric chloride ($FeCl_3$) was obtained from Sigma Chemical Co., Ltd (Saint Louis, MO, USA). CpG (5′-TCCATGACGTTCCTGACGTT-3′), FAM-labeled CpG (CpG-FAM) and RT-PCR primers were provided by Sangon Biotech Co., Ltd (Shanghai, China). Dimethyl sulphoxide (DMSO), dipotassium ethylene diamine tetraacetate (EDTA-2 K), and urea were obtained from Sinopharm Chemical Reagent Co., Ltd (Shanghai, China). Roswell park memorial institute 1640 medium (RPMI-1640), Dulbecco's Modified Eagle Medium (DMEM), penicillin-streptomycin solution, fetal bovine serum (FBS), 3-(4,5- dimethylthiazol-2-yl)−2,5-diphenyltetrazolium bromide (MTT), and phosphate buffered saline (PBS) were purchased from Gibco Life Technologies (Gaithersburg, MD, USA). ECL chemiluminescence detection kit and denaturing polyacrylamide gel electrophoresis (dPAGE) were obtained from Hunan Auragene Biotech Co., Ltd. (Hunan, China). Magna PVDF transfer membrane and BCA protein quantification kit were obtained from Beijing Dingguo Changsheng Biotech Co., Ltd (Beijing, China). IL-4 was purchased from Sino Biological Inc. (Beijing, China). TRIzol reagent, First Strand cDNA Synthesis Kit and qPCR Detection Kit were bought from Thermo Fisher Scientific Co., Ltd (MA, USA). 4′, 6-diamidino-2-phenylindole (DAPI), Lyso-Tracker Red and Hoechst33342 were bought from Solarbio Biotech, Co., Ltd (Beijing, China). DiI and DiO were provided by MaoKang Biotechnology Co., Ltd (Shanghai, China). The antibodies of CD206, CD86, CD4 and CD8 were from ABclonal Technology Co., Ltd (Wuhan, China). The antibody of CD80 was provided by Proteintech Group Inc. (Wuhan, China). The antibodies used for flow cytometry were purchased from Elabscience Biotechnology Co., Ltd (Wuhan, China). Aspartate aminotransferase assay

kit, alanine aminotransferase assay kit, urea assay kit and creatinine assay kit were obtained from Nanjing Jiancheng Bioengineering Institute (Jiangsu, China). D-Luciferin potassium salt were obtained from MedChemExpress (New Jersey, USA).

2.2. Cells

RAW264.7 cells and B16F10 cells were obtained from Xiangya Cell Center (Changsha, China). The cells were cultured in DMEM or RPMI-1640 medium supplemented with 10% FBS, 1% penicillin (50 U/ml) and streptomycin (50 U/ml) in a 5% CO_2 humidified atmosphere at 37 °C, respectively. Luciferase-tagged B16F10 (B16F10-luc) cells were kindly provided by Prof. Xiang Chen (Xiangya Hospital of Central South University), which were cultured in RPMI-1640 medium supplemented with 10% FBS, 1.5 μg/ml puromycin, 1% penicillin (50 U/ml) and streptomycin (50 U/ml).

2.3. Animals

Female C57BL/6 mice (4 to 6 weeks old) were obtained from Changzhou Cavens Laboratory Animal Co., Ltd. (Jiangsu, China). The mice were maintained in a sterile environment and allowed free access to food and water. All animal experimental procedures were approved by the Experimental Animal Ethics Committee from Xiangya School of Pharmaceutical Sciences of Central South University.

2.4. Preparation of IPI549@MOF/CpG NPs

IPI549 nanocore was prepared by quickly adding 50 μl IPI549 DMSO solution (10 mg/ml) to 5 ml ultrapure water under stirring and sonification (250 W). Afterwards, 50 μl tannic acid (TA) solution (40 mg/ml) and 50 μl $FeCl_3$ solution (10 mg/ml) were added under constant ultrasonication for 2 min to prepare IPI549@MOF NPs. The appearance of IPI549 nanocore and IPI549@MOF NPs were monitored for 30 min to study the colloidal stability. The concentration of IPI549 (50, 100 or 150 μg/ml) to prepare IPI549@MOF was optimized by detecting the particle size and loading capacity (LC%). Then, CpG was added and incubated for 30 min to form IPI549@MOF/CpG NPs, followed by centrifugation at 20 000 rpm for 10 min to remove the supernatant. The resulting IPI549@MOF/CpG NPs were redispersed in ultrapure water.

2.5. Characterization of IPI549@MOF/CpG NPs

The particle size and ζ potential of NPs were measured by Zetasizer Nano-ZS (Malvern Instruments, UK). The loading of CpG (with FAM-labeled) in MOF shell was verified by taking fluorescence images at 470 nm LED excitation in a dark room. To quantify CpG encapsulation, IPI549@MOF/CpG was prepared by using FAM-labeled CpG with different concentrations (1, 2 and 4 μM). The unencapsulated CpG in the supernatant was collected after centrifugation at 20,000 rpm for 10 min, and quantified using polyacrylamide gel electrophoresis (PAGE) assay at 200 V for 30 min. The gel images were recorded by a ChemiDoc XRS+ imaging system (Bio-Rad, USA). The morphology and elemental analysis of IPI549@MOF/CpG were measured by a transmission electron microscopy-energy dispersive spectrometer (TEM-EDS, Titan G2 60–300, FEI). UV–Vis absorbance spectra of TA/Fe MOF, IPI549 nanocore and IPI549@MOF/CpG were recorded using a UV–Vis spectrophotometer (UV-2600, Shimadzu, Japan). To study the colloidal stability, IPI549@MOF/CpG was incubated with water, PBS (10 mM, pH 7.4) and DMEM culture medium (containing 10% FBS), and the particle size was measured at 0, 1, 2, 4, 8, 12, 24 and 48 h. To explore the protective effect of IPI549@MOF/CpG for CpG, free CpG or IPI549@MOF/CpG was incubated with FBS (5%, 10% or 20%) at 37 °C for 3 h, followed by heating at 95 °C for 10 min to denature FBS. Then, the samples were added into Tris buffer containing EDTA and urea to release the encapsulated CpG, and PAGE electrophoresis was used to analyze the extent of CpG degradation.

2.6. Drug release study

IPI549@MOF/CpG was dispersed in 5 ml of different dissolution media (pH 7.4 PBS buffer and pH 5.5 PBS buffer). All samples were then placed in a constant temperature shaker (100 rpm, 37 °C). Samples were collected at different time points (0, 1, 2, 4, 8, 12 and 24 h) and centrifuged at 3000 rpm for 10 min. The precipitation was dissolved in acetonitrile and filtered with a 0.45 μm poly (vinylidene difluoride) filter using high-performance liquid chromatography (HPLC, Agilent 1260 Infinity II).

2.7. Polarization of macrophages into M2 phenotype

RAW264.7 cells were cultured in the 6-well plates (2×10^5 cells per well) and incubated with different concentration of IL-4 (0, 1, 10, 50 and 100 ng/ml) for 24 h, and the IL-4 concentration was optimized by detecting CD206 expression via western blot assay. Upon the optimal IL-4 concentration treatment, M2 polarization of macrophages was further characterized by measuring mRNA expression of iNOS, IL-6, IL-12, Arg-1 and IL-10.

2.8. Cytotoxicity of IPI549@MOF/CpG to RAW264.7 and B16F10 cells

RAW264.7 cells were cultured in the 96-well plates (5×10^3 cells per well), followed by IL-4 stimulation to allow M2 polarization. Then, different concentrations of IPI549@MOF/CpG were added for 48 h incubation, and the MTT assay was performed to evaluate the cell viability. The cytotoxicity of IPI549@MOF/CpG towards B16F10 was similarly measured.

2.9. Cellular uptake of IPI549@MOF/CpG

RAW264.7 cells were seeded in the 35 mm glass-bottom Petri dishes (4×10^4 cells per dish) with IL-4 stimulation for 24 h, and then incubated with free FAM-labeled CpG (termed CpG-FAM) or IPI549@MOF/CpG-FAM for 4 h. After washing trice with PBS and fixing with 4% paraformaldehyde, the cells were stained with DAPI for fluorescent imaging and observed by a confocal laser scanning microscope (CLSM, LSM780 NLO, Zeiss, Germany). To track the intracellular delivery,

the lysosome was stained with Lyso-Tracker Red (80 nM) for 30 min before CLSM observation.

2.10. M2-to-M1 repolarization of macrophages for in vitro anti-tumor effect

RAW264.7 cells were cultured in the 6-well plates (2×10^5 cells per well) with IL-4 stimulation for 24 h, followed by incubation with IPI549, IPI549@MOF, or IPI549@MOF/CpG (IPI549: 10 μg/ml) for 48 h. The morphology of the cells was observed by microscope. To measure cytokines excretion, total RNA was extracted using TRIzol Reagent, and the relative mRNA expression (iNOS, TNF-α, IL-6, IL-12, Arg-1, TGF-β, IL-10) was measured by RT-PCR. To measure the surface biomarkers, the cells were harvested and lysed in RIPA buffer, and the protein expression was measured by western blot (CD206, CD80 and CD86) or flow cytometry (CD206, CD80 and MHCII). To explore the anti-tumor effect, the cell supernatants were collected and added into B16F10 cells, followed by measuring the cell viability via MTT assay. To study the phagocytosis, the macrophages were detached as a single-cell suspension and stained with fluorescent dye DiI in serum-free medium. B16F10 cells were seeded in the 6-well plates (2×10^5 cells per well) for 24 h and harvested as a single-cell suspension for staining with fluorescent dye DiO. After washing twice with PBS, two types of cells were co-cultured for 12 h, and the phagocytosis was observed by fluorescent microscopy and flow cytometer (BD FACSVerse TM, USA).

2.11. Anti-tumor efficacy of IPI549@MOF/CpG in vivo

The tumor-bearing mice model was established by subcutaneous injection of B16F10 cells (2×10^7 cells/ml) to the right axilla of C57BL/6 mice (100 μl per mouse). When the volume of tumor reached 150 mm^3, the mice were randomly divided into four groups. Each group was injected intravenously with 100 μl different formulations on Day 0, 2, 4 and 6, respectively, including PBS, IPI549, IPI549@MOF and IPI549@MOF/CpG (IPI549: 5 mg/kg, CpG: 1 mg/kg). During treatment, the tumor volume was calculated every 2 d to assess the tumor growth curves (volume $= 0.5 \times$ length $\times$ width^2). The mice were sacrificed on Day 8, and the tumor tissues were taken photos and weighed. The tumor tissue and all of the major organs were collected for hematoxylin & eosin (H&E) staining. The tissue slides were observed using an optical microscope (Ti-S, Nikon, Japan). To study the biodistribution, the tumor-bearing C57BL/6 mice were injected with IP549 or IPI549@MOF/CpG via tail vein. Mice were sacrificed 24 h after injection. Tumor tissues and major organs were collected, weighed, and IPI549 extracted from tumor or major tissues was quantified by HPLC.

2.12. Biocompatibility of IPI549@MOF/CpG in vivo

Hemolysis test was carried out by incubating 2% (v/v) red blood cells (RBCs) with an equal volume of water, PBS or IPI549@MOF/CpG for 3 h at 37 °C. After centrifugation, the samples were taken photos and the UV–Vis absorbance at 540 nm of the supernatant was measured using a microplate reader (InfiniteM200, Tecan) to calculate the hemolysis rate. During treatments, the weight of each mouse was recorded every 2 d After treatment, the blood of mice was collected to detect a series of biochemical indexes to evaluate hepatic and renal toxicity, including alanine aminotransferase (ALT), aspartate aminotransferase (AST), creatinine (CRE), and blood urea nitrogen (BUN).

2.13. Immune responses in tumor after treatments

After treatments, IL-6, TNF-α and IL-10 in peripheral blood were analyzed using the mouse ELISA kits according to the manufacturer protocols. Tumor tissues were homogenized and added RIPA lysate to extract total proteins. The protein expression (CD206, CD80, CD4 and CD8) was measured by western blot. Meanwhile, the tumor tissues of some other mice were fixed and sliced. The immunofluorescence staining of tumor slides was imaged to evaluate the expression level of the related protein, and the cell nuclei were stained with DAPI for 15 min to localize the cells.

2.14. Anti-tumor effect of IPI549@MOF/CpG combination with aPD-L1

In this case, the tumor-bearing mice were randomly divided into four groups, each receiving one of following formulations on Day 0, 3, 6 and 9: PBS, aPD-L1, IPI549@MOF/CpG, or aPD-L1+IPI549@MOF/CpG (aPD-L1: intraperitoneal injection, the others: tail intravenous injection, [aPD-L1] = 7.5 mg/kg, [IPI549] = 5 mg/kg, [CpG] = 1 mg/kg). During the treatment, the tumor volume and body weight were measured every 2 d The mice were sacrificed on Day 12, and the tumor tissues were taken photos and weighed.

2.15. Inhibition of tumor metastasis

Pulmonary metastasis model of melanoma was established by intravenous injection of 5×10^5 B16F10-luc cells into each C57BL/6 mouse on Day 0. The mice were randomly divided into four groups, each injection the following formulation on Day 1, 4, 7 and 10: PBS, aPD-L1, IPI549@MOF/CpG, or aPD-L1 + IPI549@MOF/CpG (aPD-L1: intraperitoneal injection, the others: tail intravenous injection, [aPD-L1] =7.5 mg/kg, [IPI549] = 5 mg/kg, [CpG] = 1 mg/kg). On Day 15, the mice were intraperitoneally injected with D-Luciferin potassium salt (150 mg/kg), and the bioluminescence imaging was performed using IVIS Lumina XRMS Series (PerkinElmer, Waltham, MA). Finally, the mice were sacrificed and the lung of each group was collected to observe pulmonary metastasis nodules. The H&E staining of lung sections were conducted and imaged for tumor metastasis analysis.

3. Results and discussion

3.1. Preparation and characterizations of IPI549@MOF/CpG NPs

By virtue of the extremely hydrophobic nature of IPI549, we first prepared the pure drug nano-core via a self-drug assembly strategy. Briefly, the drug was dissolved in

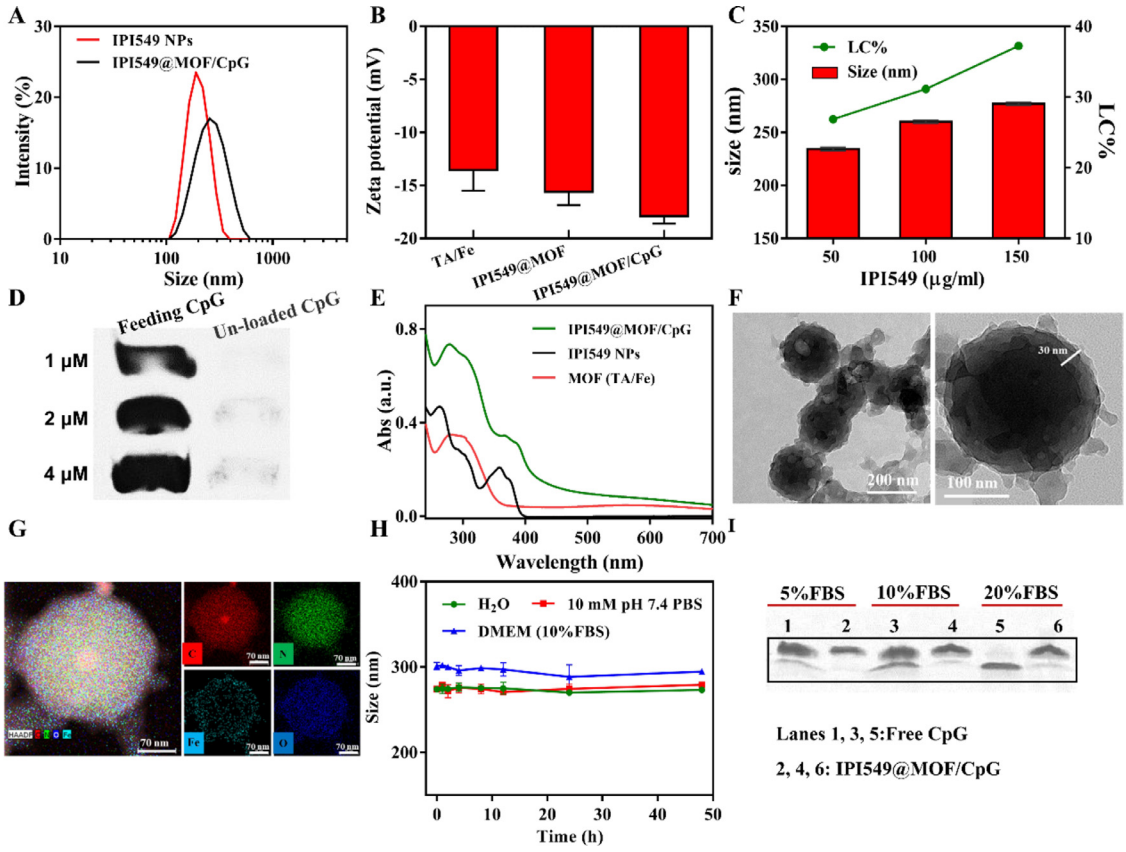

Fig. 1 – (A) DLS measurement of IPI549 NPs, IPI549@MOF/CpG. (B) ζ potential of TA/Fe MOF, IPI549@MOF and IPI549@MOF/CpG ($n = 3$). (C) Effect of IPI549 concentration on LC% and particle size of IPI549@MOF ($n = 3$). (D) PAGE gel images for characterization of CpG encapsulation into IPI549@MOF. (E) The UV–Vis spectra of TA/Fe MOF, IPI549 and IPI549@MOF/CpG. (F) TEM image and (G) element mapping images of IPI549@MOF/CpG. (H) Stability of IPI549@MOF/CpG ($n = 3$). (I) PAGE images characterization the CpG protection in 5%, 10% and 20% FBS.

DMSO solution, and dropwise added into aqueous solution under sonification. After DMSO removement, the nano-drug was formed with dynamic size ~ 190 nm (Fig. 1A, termed IPI549 NPs). The shell layer was then coated via coordination between TA and Fe^{3+} to the MOF structure [43,44], through which the CpG DNA was co-loaded. After MOF coating, the nanoparticles changed color from milky white to deep blue with size increasing to 275 nm (Fig. 1A, termed IPI549@MOF/CpG), and the colloidal stability of the NPs significantly improved owing to the MOF structure to prevent crystallization and ripening of the pure drug core (Fig. S1A). After MOF coating and CpG loading, the particle surface became more negative (Fig. 1B) because of abundant phenolic hydroxyl groups within the structure, which also benefited for enhanced colloidal stability [45]. The successful CpG loading can be easily visualized by labeling CpG with a FAM fluorophore (Fig. S1B), since the MOF structure can efficiently quench the loaded FAM fluorescence [46,47].

To quantify the drugs loading, the IPI549@MOF/CpG was centrifuged, and the drug content in supernatant was measured by HPLC and gel electrophoresis, respectively, based on which the loading capacity (LC%) was calculated. With increasing feeding IPI549 concentration from 50 to 150 μg/ml during preparation, more IPI549 was loaded accompanied by an increase of particle size (Fig. 1C). Likewise, higher feeding CpG concentration gave rise to more CpG loading. Note that the MOF shell could achieve quantitative loading of CpG at each feeding concentration as indicated by minimal DNA signal in supernatant (Fig. 1D), attributable to multiple binding forces such as metal coordination and π-π stacking. At optimal condition, the LC% of IPI549 and CpG reached 37% and 7.4% with the entrapment efficiency (EE%) to be 80% and 100%, respectively, confirming the high drug loading capacity of such nanosystem. As such, the total drug loading reached 44%, which is much higher than most traditional nanoparticles [40,48]. Next, the in vitro drug release was studied by HPLC measurement. IPI549 showed a typical pH-responsive release profile (Fig. S2), in which ~20% vs 60% drug release was observed at pH 7.4 and pH 5.5, respectively, after 24 h incubation. Such pH-triggered drug release can be ascribed to the dissociation of MOF structure at acidic pH [43,49].

We then performed a systematic characterization of the NPs. From UV–Vis spectra, the IPI549@MOF/CpG displayed the characteristic peaks from both IPI549 (~216 nm and 357 nm) and the TA/Fe MOF structure (~ 283 nm) (Fig. 1E), indicating

the core-shell structure formation. To confirm such structure, the nanoparticles were characterized by TEM, which showed a well-defined core-shell spherical structure with an average diameter of ~230 nm and the shell thickness of ~30 nm (Fig. 1F). The elemental mapping images revealed that Fe element (from MOF structure) and N element (from IPI549) mainly distributed in peripheral and central region of the nanoparticles, respectively, demonstrating the IPI549/MOF core-shell structure (Fig.1G). We then explored colloidal stability of the nanoparticles by measuring dynamic particle size under various aqueous solutions, including water, PBS and DMEM cell culturing medium (containing 10% FBS), while no obvious size change was observed over a period of 48 h (Fig. 1H). Therefore, such nanosystem possesses excellent stability in biological conditions, which is attributable to the MOF shell coating. In addition to structure stabilization and CpG encapsulation, another important role of the MOF shell is to protect CpG from enzymatic degradation, a critical issue for nucleic acids-based drugs. To examine this, free CpG or IPI549@MOF/CpG was challenged with different concentrations of FBS for 3 h, and CpG degradation was analyzed by PAGE electrophoresis via labeling the CpG with a FAM fluorophore. In 5% and 10% FBS, discrete bands were seen in free CpG lanes, indicating the digestion of CpG. Notably, CpG was completely degraded in 20% FBS. For IPI549@MOF/CpG, by contrast, minimal cleavage bands were generated even at 20% FBS, demonstrating the protection effect towards CpG (Fig. 1I).

3.2. *Intracellular delivery of IPI549@MOF/CpG into M2 macrophages*

After structural characterizations, we then explored the intracellular performances of the nanoparticles. Macrophages mainly polarize into two phenotypes by different stimuli, i.e., M1 (by LPS or IFN-γ) and M2 (IL-4 or IL-13) [50]. The target of our nanosystem is TAM, a typical M2 macrophage that occupies the greatest number of immune cells in tumor tissue. To simulate TAM, the murine macrophage cells RAW264.7 were treated with IL-4, and successful M2 activation was verified by measuring CD206 expression (Fig. 2A), an important biomarker of M2 phenotype macrophages. CD206 level gradually elevated at higher IL-4 concentrations up to 100 ng/ml. To validate M2 polarization, the expression of several other markers, including iNOS, IL-6 (markers of M1), Arg-1 and IL-10 (markers of M2), were also measured using RT-PCR. Consistently, all M2 markers increased accompanied by the decrease of M1 markers, and such defined M2 polarized cells were used in subsequent studies (Fig. 2B).

We first tested the biocompatibility of IPI549@MOF/CpG by MTT assay. Interestingly, the nanoparticles exhibited minimal cytotoxicity towards macrophages, with > 80% cells still viable even at 50 μg/ml for 48 h incubation (Fig. 2C). Likewise, the same experiment was also performed on B16F10 melanoma tumor cells, and similar result was obtained (Fig. 2D). Thus, the IPI549@MOF/CpG was highly biocompatible as it was designed to exert anti-tumor effect via modulating the functions of TAM, but rather directly damaging tumor tissue. We then studied the cellular uptake of nanoparticles by confocal laser scanning microscopy (CLSM). For convenient observation, CpG was labeled by FAM fluorophore, while cell nuclei were stained blue by DAPI for localization. Almost no fluorescent signal was observed inside cells for free CpG, since the negatively charged CpG cannot penetrate the cell membrane. For IPI549@MOF/CpG, by contrast, strong fluorescence was noticed after 4 h incubation, signifying high CpG transfection efficiency of the nanoparticles (Fig. 2E).

It is known that most nanoparticles are internalized via endocytosis, and then accumulated in endo/lysosome. To track the intracellular distribution, we further stained the endo/lysosome with red fluorescence. As expected, the FAM fluorescence of CpG was highly overlapped with red fluorescence after 1 h, producing a merged orange signal. Interestingly, the orange signal was still rather strong at prolonged incubation time of 8 h, indicating the targeted delivery of CpG in endo/lysosome (Fig. 2F). It should be noted that TLR9 is the key receptor of CpG to trigger the immune response of cells, and this receptor is located in lysosomes of macrophages [51,52]. Therefore, targeting delivery and accumulation of CpG in lysosomes facilities its binding with TLP9, which is important for immune activation.

3.3. *M2-to-M1 repolarization in vitro by IPI549@MOF/CpG to enable anti-tumor activity*

Having confirmed the effective intracellular uptake, we then explored the bio-functions of the nanoparticles inside cells. The major benefit of IPI549/CpG combination is their potential to synergistically promote M2-to-M1 repolarization of TAM for tumor immunotherapy. To demonstrate this hypothesis, several experiments have been performed. For IL-4 mediated M2 polarization, the cells exhibited a flattened and expanded phenotype (Fig. S3). Upon treatment with different drug-containing formulations, the cells became smaller and rounded, some of which adopted an elongated spindle-shaped appearance, which suggests M1 repolarization [53]. Notably, compared with free IPI549 and IPI549@MOF (the nanosystem without CpG loading), the co-delivery system of IPI549@MOF/CpG showed the most pronounced influence on cell morphology change, suggesting a synergistic effect between these two drugs. To directly probe the M2-to-M1 phenotype switch, representative biomarkers of iNOS (M1 phenotype biomarker) and Arg-1 (M2 phenotype biomarker) were quantified. After drug treatments, the expression of iNOS obviously upregulated companied by decrease of Arg-1, with the efficacy of IPI549@MOF/CpG > IPI549@MOF > free IPI549 (Fig. 3A and 3B).

It is known that the M1 polarized macrophages play multiple roles in anti-tumor immune response due to its capability of cytokine secretion, antigen presentation, and cell engulfment. We next explored all these functions of the macrophages after treatment with IPI549@MOF/CpG. The M2 macrophages (induced by IL-4) mainly expressed anti-inflammatory cytokines of IL-10, TGF-β (Fig. 3A and 3B), which are immunosuppressive cytokines in tumors. IL-10 could promote tumor proliferation while TGF-β inhibits the activation of anti-tumor immune response, both of which facilitate the progress of tumor [54]. With drugs treatment, these two anti-inflammatory cytokines were markedly suppressed, and concomitantly, the pro-inflammatory

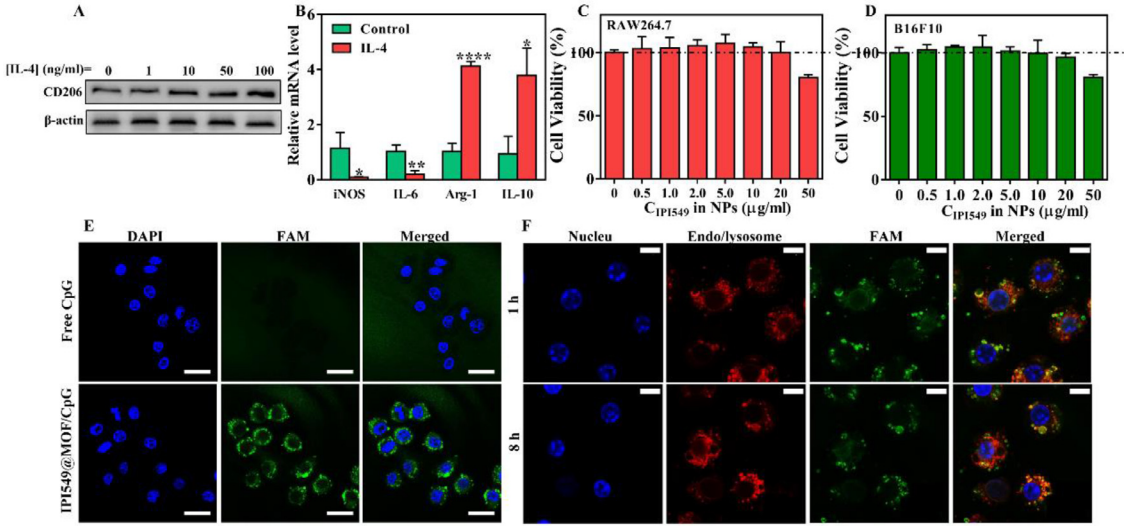

Fig. 2 – (A) The level of CD206 protein expression stimulated by various concentrations of IL-4. (B) The mRNA expression of iNOS, IL-6, IL-12, Arg-1 and IL-10 before and after treatment with 100 ng/ml IL-4 ($n = 3$). The viability of RAW264.7 cells (C) and B16F10 cells (D) after incubation with various concentrations of IPI549@MOF/CpG for 48 h ($n = 4$). (E) CLSM images of cellular uptake of free CpG and IPI549@MOF/CpG. Scale bar: 25 μm. (F) Lysosomal co-localization imaging of IPI549@MOF/CpG at 1 h and 8 h. Scale bar: 10 μm.

cytokines, e.g., TNF-α, IL-6, IL-12, significantly elevated. These three types of cytokines, on the other hand, could damage tumor by various mechanisms and induce anti-tumor immunity [55]. Therefore, the drugs exerted a positive effect on anti-tumor cytokines excretion, and in general, the IPI549@MOF/CpG group displayed the best efficacy. With the promotion of pro-inflammatory cytokines excretion, we next investigated the anti-tumor effect of these cytokines as an innate immunity. To do this, the macrophages were pre-treated with each formulation for 24 h to allow cytokines excretion, and then the cell medium was collected to treat B16F10 cells. Notably, all drug-containing groups showed anti-proliferation effect as compared with the control, and the best efficacy was achieved for IPI549@MOF/CpG (Fig. 3C), consistent with the above cytokines excretion results.

The antigen presentation capability of macrophage is highly related to its phenotype. The antigen presenting molecule of major histocompatibility complex class II (MHC II) and the co-stimulatory molecules of CD80 and CD86 play critical in antigen presentation to activate T cells. During this process, MHC II presents the engulfed antigen to T cells via specific binding with T cell receptor (TCR), and CD80/CD86 act as the second signal molecules to bind CD28 on T cells to stimulate T cells proliferation. M1 macrophages are characterized by the expression of CD80 and CD86 with high antigen presentation activity, while M2 macrophages express the biomarker of CD206. As mentioned, the macrophages induced by IL-4 displayed high level of CD206, but low expression of both CD80 and CD86 (Fig. 3D). However, this can be reversed by drugs treatments, with an obvious upregulation of CD80 and CD86, owing to M2-to-M1 repolarization. To have a quantitative understanding, the protein expression on cell membrane was then detected using flow cytometry (Fig. 3E-3H). IPI549-containing formulations could significantly reduce CD206 while increase CD80 (Fig. 3F and 3G), and again, IPI549@MOF/CpG was the most effective one. In addition, the expression of MHC II, the most important molecule in antigen presentation, also strongly elevated by IPI549 and IPI549-loaded NPs, especially for IPI549@MOF/CpG (Fig. 3H). We therefore reason that the antigen presentation capability of macrophages can be effectively enhanced after IPI549@MOF/CpG treatment by upregulation of CD80, CD86 and MHC II.

Finally, we studied the capability of macrophage to engulf tumor cells, which is important to link the innate and adaptive immune responses. The macrophage exerts innate immune via physical engulfment to directly kill tumor cells, and the engulfed tumor cells were digested to release tumor antigen for subsequent presentation to trigger adaptive anti-tumor immunity. To evaluate this process, the macrophages (red fluorescent labeled) and B16F10 tumor cells (green fluorescent labeled) were co-incubated, and visualized by confocal laser scanning microscopy (CLSM) (Fig.3I). The macrophages were pre-treated with drugs to allow M1 re-polarization. However, IPI549 stimulated cells still showed minimal phagocytosis of cancer cells, as indicated by lack of colocalization of red and green fluorescence. This can be explained that the cunning tumor cells express immune escape signals such as CD47 (a well-known “don’t-eat-me” signal), which inhibit recognition and phagocytosis of macrophages. For macrophages treated with IPI549@MOF/CpG, by contrast, a high level of fluorescence co-localization was observed, suggesting tumor cells engulfment. To quantify this result, the cell phagocytosis was further studied by flow cytometry. As positive control, the M1 macrophages showed high level of cell engulfment (Fig. S4). For M2 macrophages (with

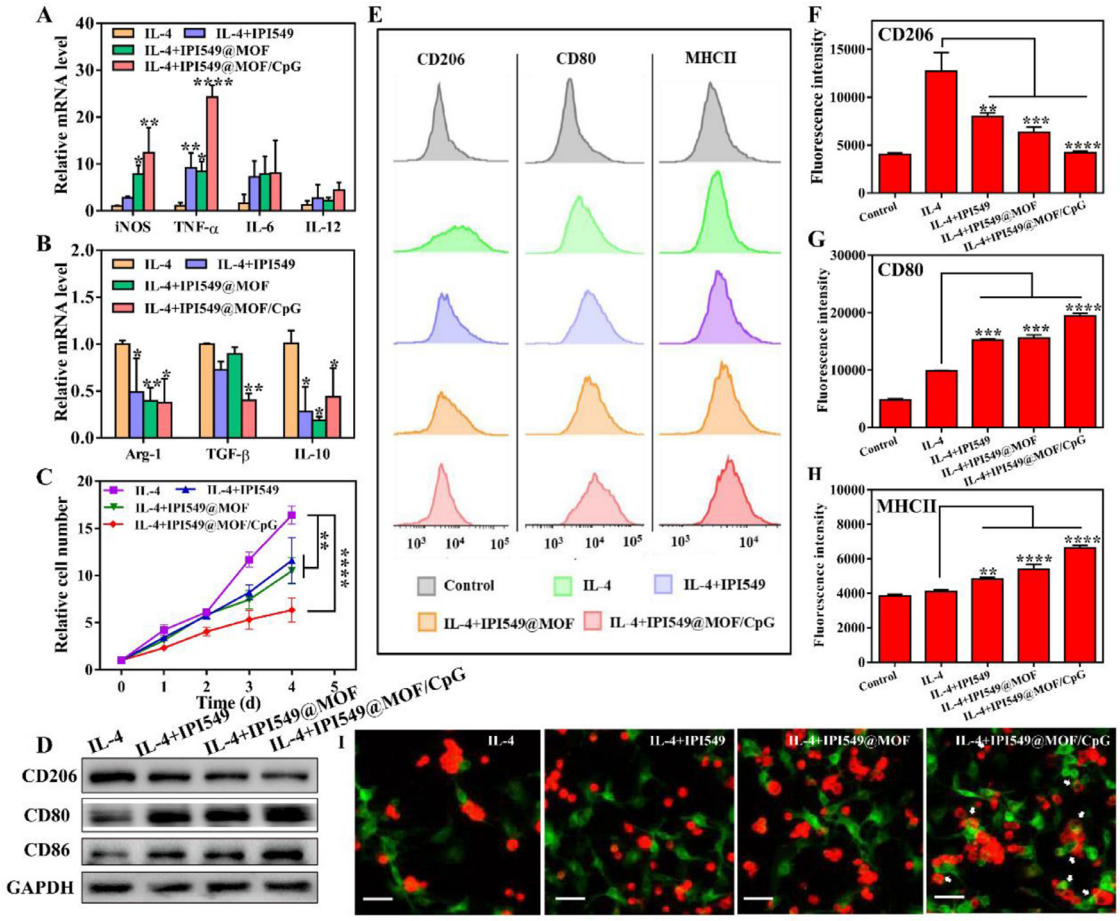

Fig. 3 – The mRNA expression of (A) iNOS, TNF-α, IL-6, IL-12 and (B) Arg-1, TGF-β, IL-10 after different treatments ($n = 3$). (C) Relative growth curves of B16F10 cells over 4 d after treatment with cell media of macrophages with different treatments ($n = 3$). (D) The protein expression of CD206, CD80 and CD86 after different treatments measured by western blot. (E) The expression of CD206, CD80 and MHCII on macrophages surface after various treatments measured by flow cytometry. (F-H) Fluorescence intensity quantified from D ($n = 3$). (I) The fluorescence images showing phagocytosis of B16F10 cells (green) by macrophages (red). Scale bar: 50 μm. (For interpretation of the references to colour in this figure legend, the reader is referred to the web version of this article.)

IL-4 pretreatment), however, the phagocytosis was much lower. Among various treatments, only IPI549@MOF/CpG could promote significant cell phagocytosis, consistent with the above result. This can be attributed to the CpG co-loading, since previous work has demonstrated that CpG evokes changes in central carbon metabolism of macrophage and thus potentiate cancer cells engulfment by overcoming CD47-mediated "don't-eat-me" signal [42]. Collectively, all these experiments demonstrated that the anti-tumor activities of IPI549@MOF/CpG were achieved by M2-to-M1 macrophage reprograming to promote the excretion of anti-tumor cytokines, tumor engulfment and antigen presentation.

3.4. *In vivo anti-tumor efficacy of IPI549@MOF/CpG*

Next, we explored the *in vivo* anti-tumor efficacy of the nanoparticles by using tumor-bearing C57BL/6 mice model through subcutaneous injection of B16F10 cells. Prior to intravenous injection of the nanoparticles, the hemocompatibility was tested. With up to 200 μg/ml IPI549@MOF/CpG, less than 5% of hemolysis was observed (Fig. S5), indicating high biosafety of the nanoparticles for intravenous injection. The biodistribution of the nanoparticles was also studied by measuring IPI549 concentration (Fig. S6). Notably, IPI549@MOF/CpG achieved significantly higher drug concentration in tumor than free IPI549, demonstrating the tumor targetability of the nanoparticles. For in vivo treatment, the mice were randomly divided into four groups ($n = 5$), each receiving 100 μl PBS, IPI549, IPI549@MOF or IPI549@MOF/CpG (5 mg/kg IPI549, 1 mg/kg CpG), respectively, by tail vein injection on Day 0, 2, 4 and 6. The general anti-tumor effect was dynamically evaluated by measuring tumor volume every other day. Compared with the control, moderate tumor inhibition was seen for free IPI549 and IPI549@MOF, while the best

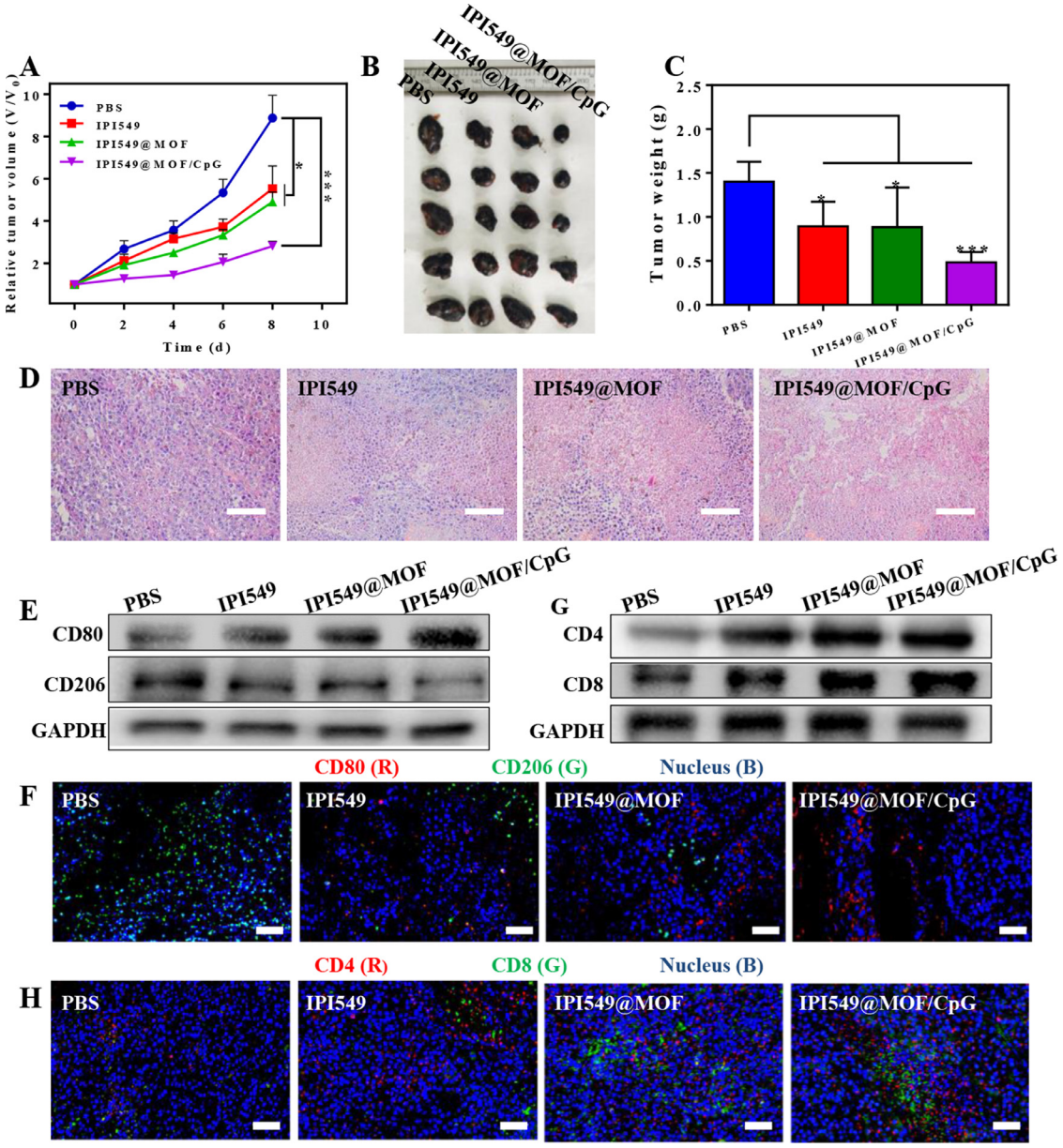

Fig. 4 – (A) The relative tumor growth curves during different treatments over a period of 8 d ($n = 5$). (B) The representative photographs of the excised tumors. (C) The tumor weight at Day 8 after various treatments ($n = 5$). (D) H&E staining of tumor sections. Scale bar: 200 μm. (E) The expression of CD80 and CD206 protein in tumor tissues after different treatments. (F) The immunofluorescence images of CD80 and CD206 in tumor tissues. Scale bar: 50 μm. (G) The expression of CD4 and CD8 proteins in tumor tissue after different treatments. (H) The immunofluorescence images of CD4 and CD8 in tumor tissues. Scale bar: 50 μm.

efficacy was observed for IPI549@MOF/CpG (Fig. 4A). For direct observation, the tumor tissue was extracted after treatment, and the tumor weight was quantified, based on which the anti-tumor efficacy was obtained with order of free IPI549 < IPI549@MOF < IPI549@MOF/CpG (Fig. 4B and 4C). The tumor tissue was then pathologically examined by HE staining, in which the highest level of nuclear necrosis and cavitation were observed for IPI549@MOF/CpG group (Fig. 4D), in line with the above results.

Given such efficacy, we then investigated the anti-tumor mechanisms. To confirmed the M1 macrophage polarization and enhanced antigen presentation, the representative biomarkers, i.e., CD80 and CD206, were detected by western blot and immunofluorescence. With PBS treatment, TAMs were mainly M2 polarized with high level of CD206, while IPI549@MOF/CpG could re-educate the TAMs towards M1 phenotype with an obvious upregulation of CD80 (Fig. 4E and 4F). In addition, the typical cytokines were measured (Fig. S7). Compared with the control, IL-10 significantly decreased, whereas IL-6 and TNF-α dramatically increased, confirming M2-to-M1 phonotype switch. Macrophage is the primary antigen presenting cells, and re-education TAMs is a highly

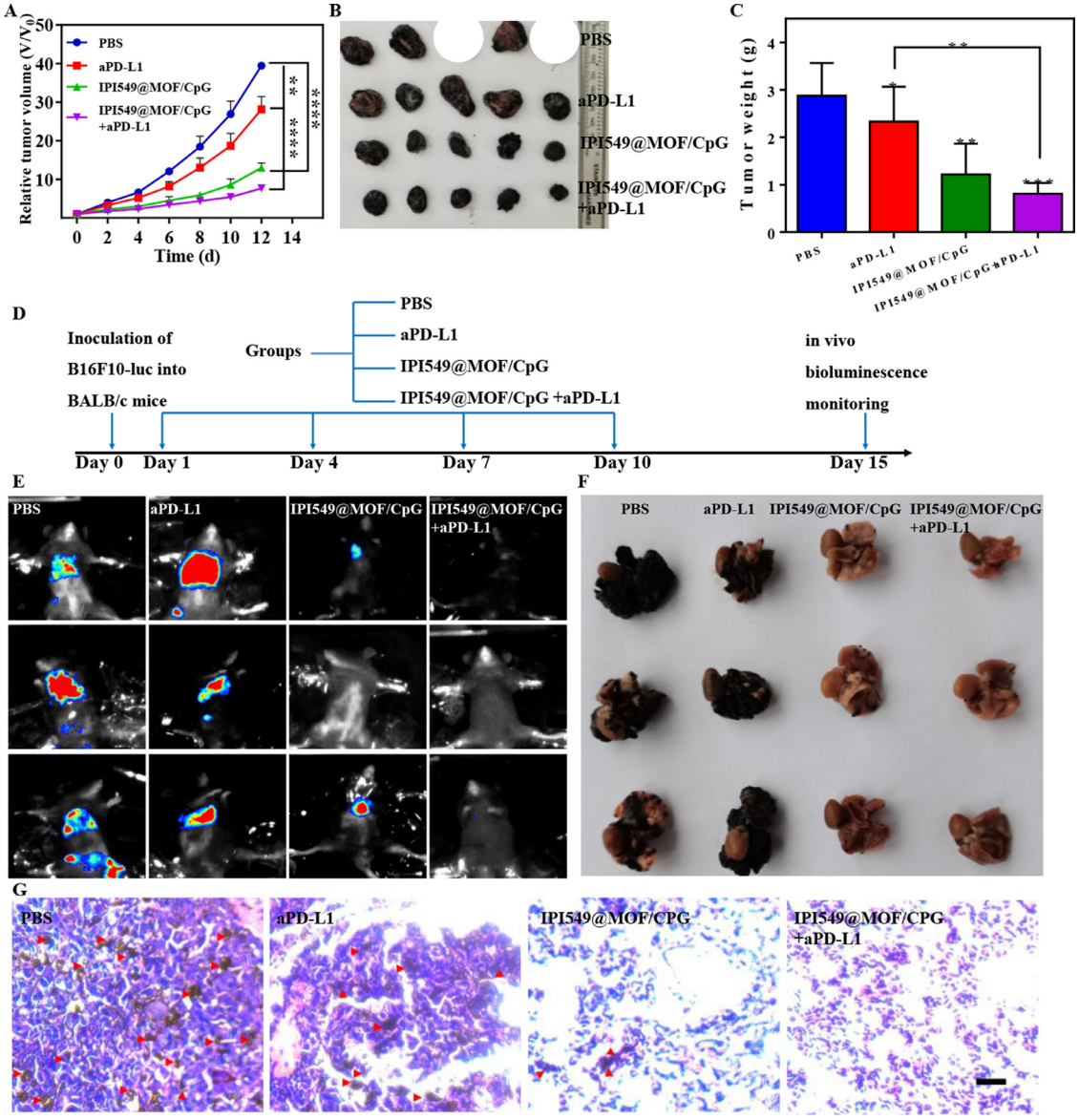

Fig. 5 – (A) The relative tumor growth curves during different treatments over a period of 12 d ($n = 5$). (B) The representative photographs of the excised tumors. (C) The tumor weight on Day 12 after various treatments ($n = 5$). (D) The schematic process of pulmonary metastasis B16F10-luc tumor with various treatments. (E) Bioluminescence imaging of the B16F10-luc lung metastasis after different treatments on Day 15 ($n = 3$). (F) Photographs of pulmonary metastatic nodules in each group on Day 15 ($n = 3$). (G) H&E staining of lung sections. Red arrows indicate the tumor areas. Scale bar: 100 μm. In panel A and B, two of the five tumors exceeded 2000 mm^3 in PBS treatment group after treatment, and mice were defined as dead. Therefore, these two tumors were excluded for analysis.

promising strategy for enhanced anti-tumor immunotherapy. To validate this effect, we also studied the infiltration of CD4+ and CD8+ T cell, the final effector immune cells, by measuring CD4 and CD8 expression. For PBS control, the tumor tissue presented low level of CD4/CD8 expression (Fig. 4G&4H), indicating the lack of T cells infiltration owing to the immunosuppressive tumor microenvironment. On the contrary, the CD4/CD8 expression was enhanced by IPI549@MOF/CpG treatment. Therefore, our nanosystem could target and re-program TAMs to enhance their antigen presenting capability, and then recruit T cells infiltration for activation, thus acting as a bridge to promote both innate and adaptive immune response.

Meanwhile, the biocompatibility of the nanosystem was evaluated. The body weight of mice almost unchanged during treatments (Fig. S8), indicating no acute toxicity. The serum samples were collected after treatments to measure the biochemical indexes, and both hepatic function indexes and renal function indexes were within the normal range (Fig. S9), suggesting no hepatotoxicity and nephrotoxicity. The main organs were further analyzed by HE staining, in which none of them showed any pathological changes (Fig. S10). Overall, our

nanosystem was highly biocompatible owing to its nontoxic nature.

3.5. *IPI549@MOF/CpG combination with aPD-L1 for enhanced immunotherapy and tumor metastasis inhibition*

Stimulated by the promotion of T cells infiltration, we further combined the nanosystem with PD-L1 antibody (aPD-L1), a widely used ICB in melanoma therapy, for combinatorial tumor immunotherapy. In this case, the tumor-bearing C57BL/6 mice were randomly divided into four groups ($n = 5$): PBS, aPD-L1, IPI549@MOF/CpG, aPD-L1 + IPI549@MOF/CpG (aPD-L1: 7.5 mg/kg, IPI549: 5 mg/kg, CpG: 1 mg/kg), and each group was administrated on Day 0, 3, 6 and 9. Note that the monotherapy of aPD-L1 only showed marginal tumor inhibition effect (Fig. 5A-5C), due to immunosuppressive microenvironment lack of pre-infiltrated T cells [56]. This result is consistent with clinical data that the overall response rate of melanoma patients to anti-PD immunotherapy is ~30% [57]. IPI549@MOF/CpG achieved better treatment outcome than aPD-L1 by virtue of strong immune regulation effect, and notably, the efficacy was strongly enhanced when combining with aPD-L1. In this combination, IPI549@MOF/CpG regulates TAMs for antigen presentation and T cell infiltration, while aPD-L1 reinvigorate T cells to attack tumor cells, resulting in a synergistic anti-tumor effect.

For melanoma in clinic, metastasis is the main cause of patient death and remains a formidable challenge for cancer treatment. Fortunately, the immunotherapy provides a promising strategy to combat tumor metastasis by virtue of this systematic immune response to damage both primary and distant tumor and prevent tumor metastasis [58]. Encouraged by the excellent immune regulation effect of the nanoparticles, we then investigated the capability to inhibit tumor metastasis, the main cause of death for most melanoma patients. As a proof-of concept, pulmonary metastasis tumor model was established by intravenous injection of B16F10-luc cells. Then, the mice were treated with PBS, aPD-L1, IPI549@MOF/CpG, or aPD-L1+IPI549@MOF/CpG (aPD-L1: 7.5 mg/kg, IPI549: 5 mg/kg, CpG: 1 mg/kg) on Day 1, 4, 7 and 10. On Day 15, bioluminescence imaging was performed for efficacy evaluation (Fig. 5D). For PBS group, a high bioluminescence intensity was observed at lung tissue (Fig. 5E), suggesting the successful establishment of the lung metastasis model. Monotherapy of aPD-L1 had little inhibition effect on lung metastasis because immune response caused by the antibody was fairly weak. IPI549@MOF/CpG suppressed more lung metastasis than aPD-L1 did as its TAM modulation to induce immune response. In accordance with the primary tumor inhibition effect, IPI549@MOF/CpG combination with aPD-L1 demonstrated significant suppression on lung metastasis, which can be attributable to the synergistic effect on macrophage programing, T cell infiltration, as well as immune checkpoint blockage.

Next, the lung tissue was collected to analyze the metastasis loci, in which the results were consistent with the corresponding luminescence image (Fig. 5F), confirming that the combination therapy could effectively inhibit lung metastasis. Specifically, abundant pulmonary metastasis nodules were observed in PBS group as evidenced by the accumulation of black colored melanoma cells. However, no noticeable metastasis nodules were seen in the combinatorial immunotherapy group. To confirm this, each lung tissue was further evaluated by HE staining, where the lung metastasis areas were pointed out by red arrows (Fig. 5G). Likewise, both IPI549@MOF/CpG and IPI549@MOF/CpG + aPD-L1 achieved remarkable inhibition of lung metastasis, which is originated from their capability to simultaneously activate innate and adaptive immune responses.

4. Conclusion

In summary, we designed and fabricated a non-cytotoxic nanomedicine co-delivering IPI549 and CpG to re-educate TAM for tumor immunotherapy. The nanoparticles were prepared through a facile self-assembly process with core-shell structure. Such nanosystem is advantageous for extra-high drug loading capacity, excellent colloidal stability, and protection of CpG from physiological degradation. By virtue of endocytosis uptake pathway, the nanoparticles could effectively deliver CpG into lysosomes for TLR9 binding, which combines with IPI549 to switch M2 macrophages to M1 phenotypes. The repolarized M1 macrophages display multiple anti-tumor effect, such as excretion of tumor killing cytokines, up-regulation of CD80/CD86 and MHC II to enable antigen presentation. Notably, while M2-to-M1 repolarization strategy has been extensively explored previously [50], the antigen presentation is still poor in most case because of the lack of tumor antigen exposure. Here we explicitly solved this problem by promoting macrophage phagocytosis of tumor cells. This is achieved owing to the metabolic rewiring of macrophage by CpG to overcome CD47-mediated “don’t-eat-me” signal. The engulfed tumor cells would release tumor antigens inside macrophages for effective presentation. In vivo, the nanoparticles achieved a notable anti-tumor effect via M2-to-M1 reprograming and cytotoxic T lymphocytes infiltration, which synergized with aPD-L1 to effectively inhibit both primary tumor growth and metastasis with excellent biocompatibility. Given the high abundance of macrophages in various types of solid tumor and their close relationship with tumor progress, such biocompatible nanomedicine shows great promise as immunotherapeutic agent to treat tumor.

Conflicts of interest

The authors declare no competing financial interest.

Acknowledgments

This work was supported by National Natural Science Foundation of China (Nos. 21804144, 81974000, U1903125, 82073799), Natural Science Foundation of Hunan province in China (Nos. 2021JJ10077, 2021JJ20084, 2022JJ30903), Natural Science Foundation of Changsha City in Hunan province,

China (No. kq2202421) and the Science and Technology Innovation Program of Hunan Province (No. 2021RC3020).

Supplementary materials

Supplementary data associated with this article can be found, in the online version, at 10.1016/j.ajps.2022.06.001.

REFERENCES

[1] Yang B, Gao J, Pei Q, Xu HX, Yu HJ. Engineering prodrug nanomedicine for cancer immunotherapy. Adv Sci 2020;7(23):2002365.
[2] Syn NL, Teng MWL, Mok TSK, Soo RA. De-novo and acquired resistance to immune checkpoint targeting. Lancet Oncol 2017;18(12):E731–EE41.
[3] Goldberg MS. Improving cancer immunotherapy through nanotechnology. Nat Rev Cancer 2019;19(10):587–602.
[4] Buss CG, Bhatia SN. Nanoparticle delivery of immunostimulatory oligonucleotides enhances response to checkpoint inhibitor therapeutics. Proc Natl Acad Sci U S A 2020;117(24):13428–36.
[5] Yang LN, Sun J, Liu Q, Zhu RR, Yang QN, Hua JH, et al. Synergetic functional nanocomposites enhance immunotherapy in solid tumors by remodeling the immunoenvironment. Adv Sci 2019;6(8):1802012.
[6] Binnewies M, Roberts EW, Kersten K, Chan V, Fearon DF, Merad M, et al. Understanding the tumor immune microenvironment (TIME) for effective therapy. Nat Med 2018;24(5):541–50.
[7] Peng SJ, Xiao FF, Chen MW, Gao HL. Tumor-microenvironment-responsive nanomedicine for enhanced cancer immunotherapy. Adv Sci 2022;9(1):2103836.
[8] Li Q, Zhang D, Zhang J, Jiang Y, Song AX, Li ZH, et al. A three-in-one immunotherapy nanoweapon via cascade-amplifying cancer-immunity cycle against tumor metastasis, relapse, and postsurgical regrowth. Nano Lett 2019;19(9):6647–57.
[9] Wang YQ, Wang ZH, Chen BL, Yin QQ, Pan MJ, Xia HM, et al. Cooperative self-assembled nanoparticle induces sequential immunogenic cell death and Toll-like receptor activation for synergistic chemo-immunotherapy. Nano Lett 2021;21(10):4371–80.
[10] Ovais M, Guo MY, Chen CY. Tailoring nanomaterials for targeting tumor-associated macrophages. Adv Mater 2019;31(19):1808303.
[11] Cassetta L, Pollard JW. Targeting macrophages: therapeutic approaches in cancer. Nat Rev Drug Discov 2018;17(12):887–904.
[12] Ginhoux F, Schultze JL, Murray PJ, Ochando J, Biswas SK. New insights into the multidimensional concept of macrophage ontogeny, activation and function. Nat Immunol 2016;17(1):34–40.
[13] Zhao M, Li J, Liu JW, Xu MX, HR Ji, Wu SW, et al. Charge-switchable nanoparticles enhance Cancer immunotherapy based on mitochondrial dynamic regulation and immunogenic cell death induction. J Control Release 2021;335:320–32.
[14] Komohara Y, Fujiwara Y, Ohnishi K, Takeya M. Tumor-associated macrophages: potential therapeutic targets for anti-cancer therapy. Adv Drug Deliv Rev 2016;99(Pt B):180–5.
[15] Noy R, Pollard JW. Tumor-associated macrophages: from mechanisms to therapy. Immunity 2014;41(1):49–61.
[16] Lin YX, Xu JX, Lan HY. Tumor-associated macrophages in tumor metastasis: biological roles and clinical therapeutic applications. J Hematol Oncol 2019;12(1):76.
[17] Zhang YR, Luo JQ, Zhang JY, Miao WM, Wu JS, Huang H, et al. Nanoparticle-enabled dual modulation of phagocytic signals to improve macrophage-mediated cancer immunotherapy. Small 2020;16(46):2004240.
[18] Xia YQ, Rao L, Yao HM, Wang ZL, Ning PB, Chen XY. Engineering macrophages for cancer immunotherapy and drug delivery. Adv Mater 2020;32(40):2002054.
[19] Nywening TM, Wang-Gillam A, Sanford DE, Belt BA, Panni RZ, Cusworth BM, et al. Targeting tumour-associated macrophages with CCR2 inhibition in combination with FOLFIRINOX in patients with borderline resectable and locally advanced pancreatic cancer: a single-centre, open-label, dose-finding, non-randomised, phase 1b trial. Lancet Oncol 2016;17(5):651–62.
[20] Zhao YD, Muhetaerjiang M, An HW, Fang XH, Zhao YL, Wang H. Nanomedicine enables spatiotemporally regulating macrophage-based cancer immunotherapy. Biomaterials 2021;268:120552.
[21] Sylvestre M, Crane CA, Pun SH. Progress on modulating tumor-associated macrophages with biomaterials. Adv Mater 2020;32(13):1902007.
[22] Yue YL, Li FF, Li Y, Wang YZ, Guo XJ, Cheng ZX, et al. Biomimetic nanoparticles carrying a repolarization agent of tumor-associated macrophages for remodeling of the inflammatory microenvironment following photothermal therapy. ACS Nano 2021;15(9):15166–79.
[23] Xie R, Ruan SB, Liu JQ, Qin L, Yang CY, Tong F, et al. Furin-instructed aggregated gold nanoparticles for re-educating tumor associated macrophages and overcoming breast cancer chemoresistance. Biomaterials 2021;275:120891.
[24] Jain S, Tran TH, Amiji M. Macrophage repolarization with targeted alginate nanoparticles containing IL-10 plasmid DNA for the treatment of experimental arthritis. Biomaterials 2015;61:162–77.
[25] Shobaki N, Sato Y, Suzuki Y, Okabe N, Harashima H. Manipulating the function of tumor-associated macrophages by siRNA-loaded lipid nanoparticles for cancer immunotherapy. J Control Release 2020;325:235–48.
[26] Feng MY, Jiang W, Kim BYS, Zhang CC, Fu YX, Weissman IL. Phagocytosis checkpoints as new targets for cancer immunotherapy. Nat Rev Cancer 2019;19(10):568–86.
[27] Liu XJ, Pu Y, Cron K, Deng LF, Kline J, Frazier WA, et al. CD47 blockade triggers T cell-mediated destruction of immunogenic tumors. Nat Med 2015;21(10):1209–15.
[28] Chen QJ, Sun T, Jiang C. Recent advancements in nanomedicine for 'cold' tumor immunotherapy. Nanomicro Lett 2021;13(1):92.
[29] Duan XP, Chan C, Lin WB. Nanoparticle-mediated immunogenic cell death enables and potentiates cancer immunotherapy. Angew Chem Int Ed Engl 2019;58(3):670–80.
[30] Chen Q, Chen MC, Liu Z. Local biomaterials-assisted cancer immunotherapy to trigger systemic antitumor responses. Chem Soc Rev 2019;48(22):5506–26.
[31] Rong L, Zhang Y, Li WS, Su ZG, Fadhil JI, Zhang C. Iron chelated melanin-like nanoparticles for tumor-associated macrophage repolarization and cancer therapy. Biomaterials 2019;225:119515.
[32] Huang YJ, Guan ZL, Dai XL, Shen YF, Wei Q, Ren LL, et al. Engineered macrophages as near-infrared light activated drug vectors for chemo-photodynamic therapy of primary and bone metastatic breast cancer. Nat Commun 2021;12(1):4310.
[33] Chen Q, Chen JW, Yang ZJ, Xu J, Xu LG, Liang C,

et al. Nanoparticle-enhanced radiotherapy to trigger robust cancer immunotherapy. Adv Mater 2019;31(10):1802228.
[34] Chao Y, Xu LG, Liang C, Feng LZ, Xu J, Dong ZL, et al. Combined local immunostimulatory radioisotope therapy and systemic immune checkpoint blockade imparts potent antitumour responses. Nat Biomed Eng 2018;2(8):611–21.
[35] Saeed M, Gao J, Shi Y, Lammers T, Yu HJ. Engineering nanoparticles to reprogram the tumor immune microenvironment for improved cancer immunotherapy. Theranostics 2019;9(26):7981–8000.
[36] Dai Z, Tang J, Gu ZY, Wang Y, Yang Y, Yang YN, et al. Eliciting immunogenic cell death via a unitized nanoinducer. Nano Lett 2020;20(9):6246–54.
[37] Mosquera MJ, Kim S, Zhou H, Jing TT, Luna M, Guss JD, et al. Immunomodulatory nanogels overcome restricted immunity in a murine model of gut microbiome-mediated metabolic syndrome. Sci Adv 2019;5(3):eaav9788.
[38] Yu M, Duan XH, Cai YJ, Zhang F, Jiang SQ, Han SS, et al. Multifunctional nanoregulator reshapes immune microenvironment and enhances immune memory for tumor immunotherapy. Adv Sci 2019;6(16):1900037.
[39] De Henau O, Rausch M, Winkler D, Campesato LF, Liu CL, Hirschhorn-Cymerman D, et al. Overcoming resistance to checkpoint blockade therapy by targeting PI3K gamma in myeloid cells. Nature 2016;539(7629):443–7.
[40] Zhang XQ, Shen LM, Liu Q, Hou L, Huang LA. Inhibiting PI3 kinase-gamma in both myeloid and plasma cells remodels the suppressive tumor microenvironment in desmoplastic tumors. J Control Release 2019;309:173–80.
[41] Klinman DM. Immunotherapeutic uses of CpG oligodeoxynucleotides. Nat Rev Immunol 2004;4(4):249–58.
[42] Liu MG, O'Connor RS, Trefely S, Graham K, Snyder NW, Beatty GL. Metabolic rewiring of macrophages by CpG potentiates clearance of cancer cells and overcomes tumor-expressed CD47-mediated 'don't-eat-me' signal. Nat Immunol 2019;20(3):265–75.
[43] Liu P, Liu XJ, Cheng Y, Zhong SH, Shi XY, Wang SF, et al. Core-shell nanosystems for self-activated drug-gene combinations against triple-negative breast cancer. ACS Appl Mater Interfaces 2020;12(48):53654–64.
[44] Shen GZ, Xing RR, Zhang N, Chen CJ, Ma GH, Yan XH. Interfacial cohesion and assembly of bioadhesive molecules for design of long term stable hydrophobic nanodrugs toward effective anticancer therapy. ACS Nano 2016;10(6):5720–9.
[45] Liu P, Shi XY, Zhong SH, Peng Y, Qi Y, Ding JS, et al. Metal-phenolic networks for cancer theranostics. Biomater Sci 2021;9(8):2825–49.
[46] Schrimpf W, Ossato G, Hirschle P, Wuttke S, Lamb DC. Investigation of the co-dependence of morphology and fluorescence lifetime in a metal-organic framework. Small 2016;12(27):3651–7.
[47] Wang B, Wang PL, Xie LH, Lin RB, Lv J, Li JR, et al. A stable zirconium based metal-organic framework for specific recognition of representative polychlorinated dibenzo-p-dioxin molecules. Nat Commun 2019;10:3861.
[48] Jiang M, He KY, Qiu T, Sun JH, Liu Q, Zhang XQ, et al. Tumor-targeted delivery of silibinin and IPI-549 synergistically inhibit breast cancer by remodeling the microenvironment. Int J Pharm 2020;581:119239.
[49] Liu T, Liu WL, Zhang MK, Yu WY, Gao F, Li CX, et al. Ferrous-supply-regeneration nanoengineering for cancer-cell-specific ferroptosis in combination with imaging-guided photodynamic therapy. ACS Nano 2018;12(12):12181–92.
[50] Song Y, Huang Y, Zhou F, Ding J, Zhou W. Macrophage-targeted nanomedicine for chronic diseases immunotherapy. Chin Chem Lett 2021;33(2):597–612.
[51] Krieg AM. Therapeutic potential of Toll-like receptor 9 activation. Nat Rev Drug Discov 2006;5(6):471–84.
[52] Qu YJ, Ju Y, Cortez-Jugo C, Lin ZX, Li SY, Zhou JJ, et al. Template-mediated assembly of DNA into microcapsules for immunological modulation. Small 2020;16(37):e2002750.
[53] McWhorter FY, Wang TT, Nguyen P, Chung T, Liu WF. Modulation of macrophage phenotype by cell shape. Proc Natl Acad Sci U S A 2013;110(43):17253–8.
[54] Biswas SK, Mantovani A. Macrophage plasticity and interaction with lymphocyte subsets: cancer as a paradigm. Nat Immunol 2010;11(10):889–96.
[55] Shan H, Dou WL, Zhang Y, Qi M. Targeted ferritin nanoparticle encapsulating CpG oligodeoxynucleotides induces tumor-associated macrophage M2 phenotype polarization into M1 phenotype and inhibits tumor growth. Nanoscale 2020;12(43):22268–80.
[56] Tumeh PC, Harview CL, Yearley JH, Shintaku IP, Taylor EJM, Robert L, et al. PD-1 blockade induces responses by inhibiting adaptive immune resistance. Nature 2014;515(7528):568–71.
[57] Topalian SL, Hodi FS, Brahmer JR, Gettinger SN, Smith DC, McDermott DF, et al. Safety, activity, and immune correlates of anti-PD-1 antibody in cancer. N Engl J Med 2012;366(26):2443–54.
[58] Zhang W, Wang F, Hu C, Zhou Y, Gao HL, Hu J. The progress and perspective of nanoparticle-enabled tumor metastasis treatment. Acta Pharm Sin B 2020;10(11):2037–53.